Comparison of Coaxial Magnetic Gears Using Rare Earth and Nonrare Earth Permanent Magnets

Byeong-Cheol Bae, Seung-Hun Lee, So-Yeon Im, and Myung-Seop Lim, *Senior Member, IEEE*

Abstract*—Coaxial magnetic gears (CMGs) enable contactless torque transmission, addressing the noise and maintenance drawbacks of mechanical gears. However, the heavy reliance on rare earth permanent magnets (PMs) presents a challenge owing to their unstable supply and fluctuating costs. To mitigate dependence on rare earth PMs, this study proposes and evaluates four CMG configurations combining NdFeB and Ferrite. Each configuration is optimized using two-dimensional finite element analysis (FEA), with axial leakage considered by an equivalent magnetic circuit model instead of three-dimensional (3D) FEA. The suitability of bridge geometry for each PM combination is first assessed, revealing that irrespective of the PM material, the inner bridge provides superior torque density. Comparative analyses of the electromagnetic performance and active material costs were then conducted to evaluate the feasibility of each PM configuration. The results indicate that the difference in residual flux density between the inner and outer rotor PMs influences torque density, material costs, peak-to-peak torque, and efficiency. This difference was also observed in an appropriate gap between the active part and the end cover, at which end cover loss becomes negligible. Ferrite-Nd CMG showed the highest efficiency and lowest price among the combinations of nonrare earth PMs. Finally, electromagnetic performance comparisons of NdFeB-based and Ferrite-Nd CMGs using 3D FEA and experimental validation show that while the Ferrite-Nd CMG has a lower torque density than the NdFeB-based CMG, it offers promising advantages in terms of reduced rare earth dependency, negligible housing loss, and high efficiency.

***Index Terms*—Coaxial magnetic gear (CMG), NdFeB, Ferrite, optimization, finite element analysis (FEA), housing loss.**

I. Introduction

RESEARCH has been actively conducted on coaxial magnetic gears (CMGs) that transmit power through noncontact driving. CMGs offer numerous advantages, including low noise, inherent overload protection, and elimination of tooth wear, making them a promising alternative to mechanical gears. These benefits have spurred interest in CMGs for traction applications, such as electric vehicles and aircraft, as well as for power generation applications [1], [2], [3]. However, CMGs require substantial quantities of permanent magnet (PM) materials to achieve torque levels comparable with those mechanical gears [4]. Recent fluctuations in the supply and cost of rare earth PMs, such as NdFeB and SmCo, have increased cost-related concerns, hindering broader CMG adoption [5].

Various approaches have been proposed to reduce the reliance on rare earth PMs. Aiso et al. introduced a reluctance-based CMG that eliminates PMs in high-speed rotors, thereby decreasing the dependence on rare earth materials while enhancing efficiency by avoiding PM eddy current loss in high-speed rotors [6]. Khan et al. proposed a consequent pole transverse flux CMG, that reduced PM usage and improved manufacturability [7]. However, both the consequent pole and reluctance designs require detailed analyses of vibration and noise characteristics [8], [9]. Another strategy to minimize the reliance on rare earth PMs is the use of nonrare earth PMs. Replacing rare earth PMs with nonrare earth PMs can eliminate the dependence on rare earth in CMG. Johnson et al. optimized surface-mounted CMGs with NdFeB and Ferrite, respectively, and compared their performance [10]. Park et al. compared CMGs using NdFeB and Ferrite to analyze the effect of magnet conductivity on efficiency and losses [11]. Most studies on CMGs using Ferrite have high efficiency owing to the reduced PM eddy current loss and leakage flux. However, because Ferrite has a lower residual magnetic flux density, CMGs with Ferrite require an increased volume to achieve torque levels comparable to those of NdFeB-based CMGs. Consequently, CMGs with Ferrite exhibit a lower torque density and cost-effectiveness than their NdFeB counterparts. Using both rare earth and nonrare earth PMs can alleviate the low torque density problem, although it does not completely eliminate the dependence on rare earth PMs. Uppalapati et al. compared flux-focusing CMGs utilizing NdFeB, Ferrite, and hybrid configurations, with NdFeB and Ferrite as the inner and outer rotor PMs, respectively [12]. Al-Qarni et al. proposed a flux-focusing CMG with NdFeB in the outer rotor and a blend of NdFeB and Ferrite in the inner rotor PMs [13]. Although flux-focusing designs can increase PM utilization, they typically yield lower torque density than surface-mounted types for the same PM volume [14]. In the flux-focusing configuration, with NdFeB and Ferrite in the inner and outer rotor PMs, respectively, the torque density improves compared to Ferrite-based CMGs but remains lower than that in NdFeB-based CMGs, and the efficiency is also reduced.

Received 5 December 2024; revised 21 March 2025 and 8 November 2025; accepted 2 December 2025. Date of publication 14 January 2026; date of current version 20 July 2026. Paper 2024-EMC-1713.R2, presented at the 2023 IEEE Transportation Electrification Conference and Expo, Asia-Pacific, Chiang Mai, Thailand, Nov. 28–Dec. 01, and approved for publication in the IEEE Transactions On Industry Applications by the Electric Machines Committee of the IEEE Industry Applications Society [DOI: 10.1109/ITECAsia-Pacific59272.2023.10372332]. This work was supported by Samsung Electronics. *(Corresponding author: Myung-Seop Lim.)*

The authors are with the Department of Automotive Engineering (Automotive-Computer Convergence), Hanyang University, Seoul 04763, South Korea (e-mail: byeong@hanyang.ac.kr; seunghun6137@hanyang.ac.kr; soyeon96@hanyang.ac.kr; myungseop@hanyang.ac.kr).

Color versions of one or more figures in this article are available at https://doi.org/10.1109/TIA.2026.3653751.

Digital Object Identifier 10.1109/TIA.2026.3653751

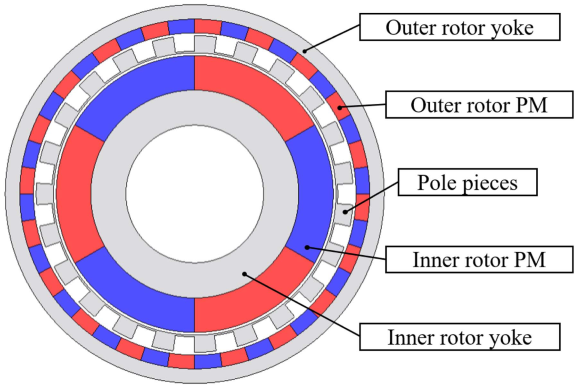

Fig. 1. Configuration of CMG (6.67:1 gear ratio).

As such, research on hybrid PM combinations is limited to flux-focusing CMGs, and there are no cases yet of combining nonrare earth PMs in the inner and rare earth PMs in the outer. Moreover, while the performance of CMGs using a single PM material has been analyzed, the characteristics that arise when the residual magnetic flux densities differ, as in hybrid PM combinations, have not been thoroughly investigated. This study aims to address the limitations, reduce dependence on rare earth materials, and explore CMG configurations with superior performance. The contributions are as follows.

- Proposal of CMGs with reduced rare earth dependence: Three surface-mounted CMG configurations using nonrare earth PMs are proposed, and their performance is compared with that of a rare earth-based CMG.
- Performance analysis of CMG according to the residual flux density of inner and outer rotor PM: A detailed analysis was conducted to determine why performance varies depending on the residual flux density of each rotor PM.
- Housing loss analysis of CMG: Analyzes the impact of housing loss on CMG performance and presents the appropriate gap between the active part and the end cover at which the end cover loss becomes negligible.

In this paper, four different combinations of NdFeB and Ferrite in the inner and outer rotors of surface-mounted CMGs are presented and their performances are compared. In a previous study presented at the *2023 IEEE Transportation Electrification Conference and Expo, Asia-Pacific (ITEC Asia-Pacific)*, four different surface-mounted CMGs with a 7:1 gear ratio were compared [15]. The integer gear ratio of 7:1 resulted in high peak-to-peak torque characteristics, which limited its usability [16]. To address this issue, this study adopts a fractional gear ratio.

The remainder of this paper is organized as follows. Section II introduces the design conditions and methods of the model. Section III evaluates whether inner, middle and outer bridges are appropriate for different PM combinations. Section IV discusses the distribution of electromagnetic performance and cost-effectiveness for different PM combinations within a range of design parameters. Section V conducts performance comparisons to validate the optimal design model with the housing. Section VI, a prototype of the NdFeB-based CMG and a potential replacement PM combination are fabricated and validated to compare their performance with that of three-dimensional (3D) finite element analysis (FEA). Finally, Section VII concludes the paper.

TABLE I
PROPERTIES OF ACTIVE MATERIALS

Active material	Residual flux density (T)	Density (kg/m^3)	Cost rate (p.u./mm^3)	Resistivity ($\Omega \cdot$ m)
NdFeB (N42H)	1.19 (@90°C)	7500	7	1.8×10^{-6}
Ferrite (FB13B)	0.43 (@90°C)	5100	1	10000
Core (50PN470)	-	7850	0.5	3.8×10^{-7}

II. Design Requirements and Process

This study examines the surface-mounted PM CMG with a 6.67:1 gear ratio, as shown in Fig. 1. The use of a fractional gear ratio primarily reduces the torque pulsation. The cogging factor, determined by the combination of the number of pole pairs and pole pieces (PPs), was calculated as follows [17]:

$$C_f = \frac{2pp_i N_s}{\mathrm{LCM}(2pp_i, N_s)} = \mathrm{GCD}(2pp_i, N_s). \tag{1}$$

where C_f is the cogging factor, pp_i is the number of inner rotor PM pole pairs, N_s is the number of PPs, LCM is the lowest common multiple, and GCD is the greatest common divisor. The smaller the C_f, the lower the peak-to-peak torque characteristics. When $pp_i = 3$, $N_s = 23$ and $pp_o = 20$, G_r, represents the gear ratio, is 6.67 and C_f is 1, satisfying the low peak-to-peak torque.

The PMs used in this design are NdFeB and Ferrite. NdFeB, a rare earth PM, has a high residual magnetic flux density but is costly. Conversely, Ferrite, a nonrare earth PM, has a comparatively low residual magnetic flux density and is more affordable. Owing to the contrasting characteristics of NdFeB and Ferrite, their combinations results in a variety of performance traits. Table I lists the details of the active materials used in the design. The possible NdFeB and Ferrite combinations are as follows:

- Nd-Nd CMG (Inner: NdFeB, Outer: NdFeB)
- Nd-Ferrite CMG (Inner: NdFeB, Outer: Ferrite)
- Ferrite-Nd CMG (Inner: Ferrite, Outer: NdFeB)
- Ferrite-Ferrite CMG (Inner: Ferrite, Outer: Ferrite)

The designs were based on the target specifications listed in Table II . The CMGs in this paper were designed for use in washing machines, intended to operate at a single speed and torque. As the outer and inner diameters were fixed values, the volumetric torque densities were determined according to the stack length that satisfied target torque.

The design variables and the ranges of the design variables are shown in Fig. 2 and Table III. The ranges of the design variables were the same regardless of the PM combination, and except for X5, the ranges were determined so that the optimal point did not reach the minimum and maximum values of the

TABLE II
TARGET SPECIFICATION

Parameters	Value	Unit
Inner pole pair	3	-
Outer rotor pole pair	20	-
Gear ratio	6.67	-
Inner rotor torque	2.52	Nm
Outer rotor torque	16.8	Nm
Inner / Outer rotor rotation speed	333.33 / 50	rpm
Outer rotor outer diameter	110	mm
Inner rotor inner diameter	48	mm

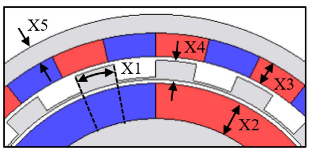

Fig. 2. Design variables of CMG.

TABLE III
RANGE OF DESIGN VARIABLES IN CMGS

PM combination	X1 (°)	X2 (mm)	X3 (mm)	X4 (mm)	X5 (mm)
Nd-Nd	5-9	6-11.5	2-3.5	3-5.5	2.5-5
Nd-Ferrite	5-9	6-11.5	2-3.5	3-5.5	2.5-5
Ferrite-Nd	5-9	6-11.5	2-3.5	3-5.5	2.5-5
Ferrite-Ferrite	5-9	6-11.5	2-3.5	2.5-5	3-5.5

design variables. Considering manufacturability, the minimum value for X5 was set at 2.5 mm. At this stage, the lengths of both the inner and outer airgaps were fixed at 0.8 mm, and the bridge thickness was set at 0.5 mm. The bridge geometry was selected by comparing the performance of the inner and outer bridges in the subsequent section.

The two-dimensional (2D) FEA results differ from the 3D FEA results owing to axial leakage flux [18]. However, because 3D FEA requires significantly more computational time than 2D FEA, many studies have relied on 2D FEA while accounting for discrepancies in the optimal design. In this optimization process, the stack length for 3D FEA was estimated by calculating the correlation coefficient between the 2D equivalent magnetic circuit (EMC), which ignores the axial leakage flux, and the 3D EMC, which incorporates the axial leakage flux path. This correlation coefficient was then used to adjust the stack length [19].

$$L_{3D,predicted} = \frac{\lambda_{2D,EMC}^2}{\lambda_{3D,EMC}^2} \cdot L_{\text{2D,FEA}} = k \cdot L_{\text{2D,FEA}}. \quad (2)$$

where $L_{3D,predicted}$ is the predicted 3D FEA stack length, $\lambda_{3D,EMC}$ is the magnetic flux calculated by the 3D EMC, $\lambda_{2D,EMC}$ is the magnetic flux calculated by the 2D EMC, $L_{\text{2D,FEA}}$ is the 2D FEA stack length, and k is the correlation coefficient. By applying the factor k, the axial leakage flux can be accounted for in 2D FEA, eliminating the need for 3D FEA.

In this study, the optimal design process follows the methodology outlined in [20]. The objective function of the optimization was to minimize the stack length and maximize efficiency, with the experimental points uniformly distributed across the design variable ranges specified in Table III. A kriging model was created from 2D FEA data that accounted for the axial leakage flux, and the optimal point was subsequently determined. A schematic of the overall optimal design process is shown in Fig. 3.

III. POSITION OF INTERCONNECTING BRIDGE

The bridge in the modulator is not desirable to increase torque density because it causes a larger leakage flux [21]. However, bridges are commonly used to enhance the manufacturability and mechanical stiffness [22]. The number of poles affects the amount of leakage flux. Therefore, the outer rotor side has a larger leakage flux than the inner rotor. For this reason, the outer bridge has more leakage flux than the inner bridge, which further reduces the torque density [23], [24]. However, these previous studies have primarily evaluated designs in which the inner and outer rotor PMs are made of the same material, with only a few research reports considering designs in which the materials are different. Therefore, this section evaluates whether an inner, middle, and outer bridge is more appropriate based on the PM combination.

When NdFeB is used in the rotor near the bridge, the magnetic flux passing through the PPs to the opposing rotor is dominant because of the sufficiently high magneto-motive force (MMF). The high MMF of the magnets near the bridge provides sufficient flux to saturate the bridge and link to the other rotor, as illustrated in Fig. 4(a) and (e). By contrast, when Ferrite was used in the rotor, the amount of flux leakage through the bridge was comparable to the flux passing through the other rotor through the PPs, as shown in Fig. 4(b) and (f). In the middle bridge configuration, as shown in Fig. 4(c) and (d), MMFs of both the inner and outer rotors affect the bridge saturation and flux leakage behavior. To verify the effect of leakage flux based on bridge location, the torque reduction rates according to bridge position were compared to the case without a bridge. Based on the model with the median design parameters in Table III : X1=7*, X2=8.75 mm, X3=2.75 mm, X4=4.25 mm, and X5=3.75 mm, the torque reduction rates for the Nd–Nd CMGs shown in Fig. 4(a), (c), and (e) are –0.21%, –2.74%, and –7.84%, respectively. Similarly, the torque reduction rates for the Ferrite–Ferrite CMGs shown in Fig. 4(b), (d), and (f) are –33.76%, –41.53%, and –63.69%, respectively. This means that the ratio of the flux leaking through the bridge to the flux linking to the opposite rotor is small for Nd-Nd and large for Ferrite-Ferrite, and it becomes larger from the inner bridge to the outer bridge.

The optimal bridge shape for each PM combination was assessed by evaluating the stack length required to satisfy the target specifications listed in Table II, within the design variable range specified in Table III. Within the design variable range, a total of 1120 experimental points were generated, consisting of 1064 points using the optimal latin hypercube design (OLHD) and 56 points generated by the sequential minimum distance design (SMDD), and the distribution of required stack lengths according to bridge position to produce the same torque is

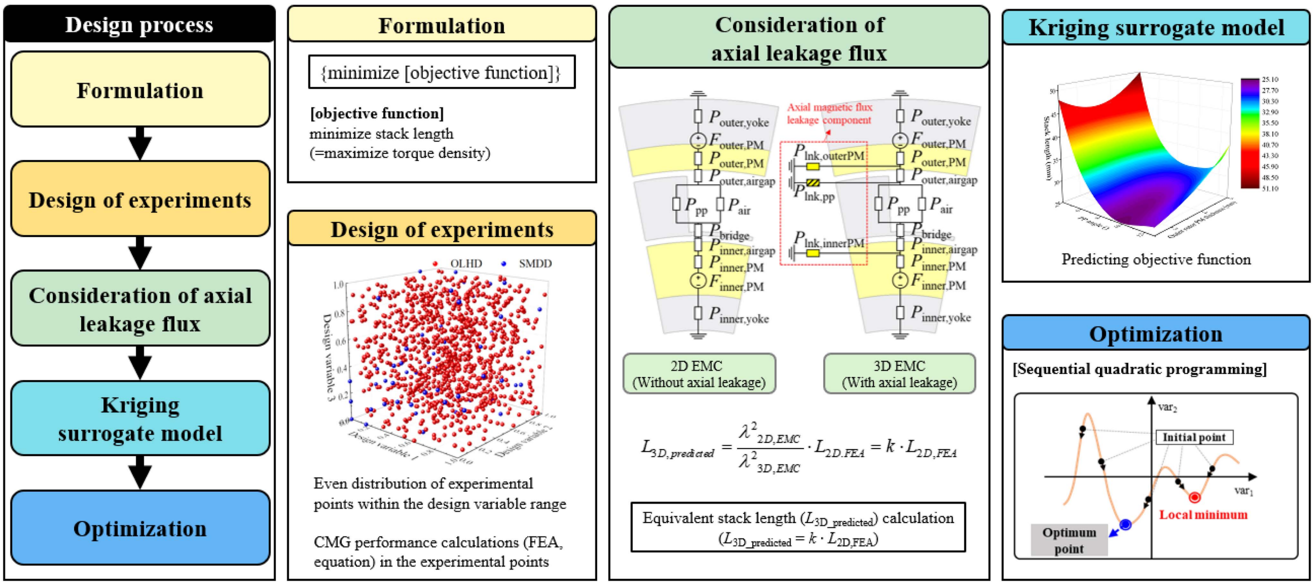

Fig. 3. Optimal design process.

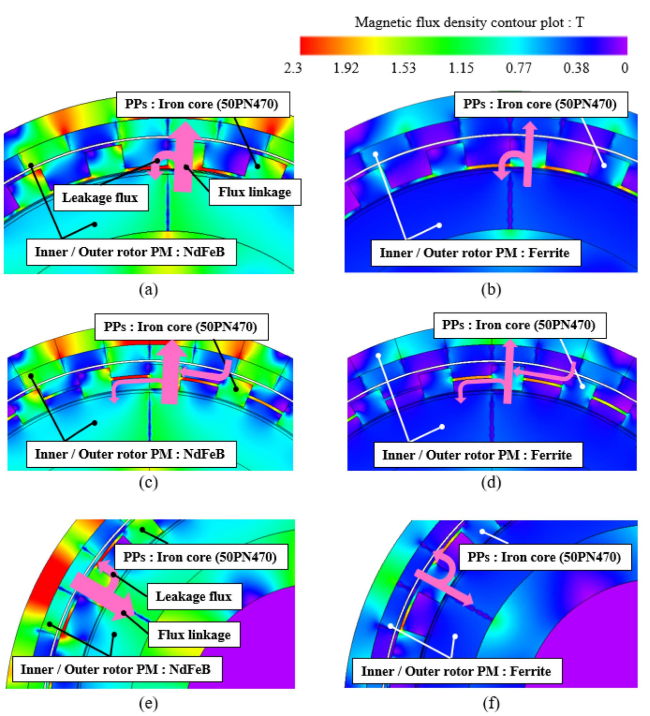

Fig. 4. Magnetic flux density distribution. (a) Nd-Nd CMG with inner bridge. (b) Ferrite-Ferrite CMG with inner bridge. (c) Nd-Nd CMG with middle bridge. (d) Ferrite-Ferrite with middle bridge. (e) Nd-Nd CMG with outer bridge. (f) Ferrite-Ferrite with outer bridge.

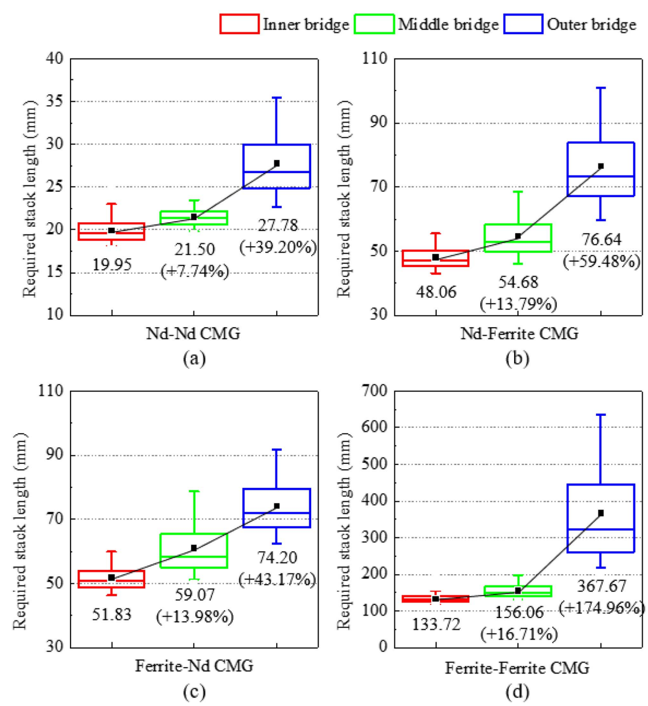

Fig. 5. Box plot of stack length distributions at identical torque levels according to bridge position. (a) Nd–Nd CMG. (b) Nd–Ferrite CMG. (c) Ferrite–Nd CMG. (d) Ferrite–Ferrite CMG.

shown in Fig. 5 as a box plot. Each box plot illustrates the data distribution, where the box indicates the interquartile range (IQR), the horizontal line denotes the median, the square marker represents the mean, and the whiskers extend to the maximum and minimum observations within 1.5 IQR. As can be seen from the average required stack length distribution in Fig. 5, the torque density decreased as the bridge was positioned on the outer side, regardless of the PM combination. It can be observed that the torque density considerably decreases when PM with lower MMF is placed closer to the bridge. As shown in Fig. 5(b) and (d), when the outer rotor PM is made of Ferrite, the required stack length for the outer bridge configuration increases by more than 60% compared to the inner bridge configuration, leading to

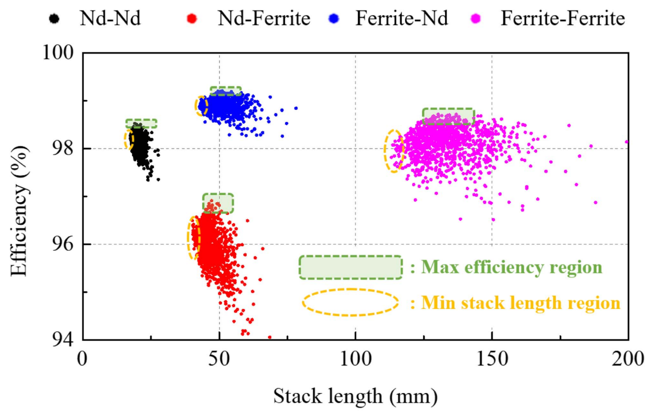

Fig. 6. Efficiency distribution by PM combination.

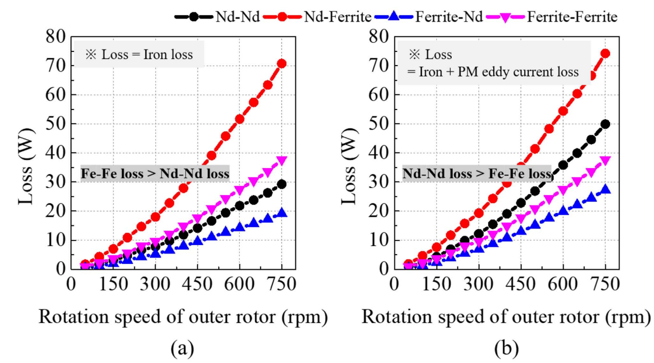

Fig. 7. Loss of CMG by PM combination according to rotation speed of outer rotor. (a) Iron loss. (b) Iron and PM eddy current loss.

a noticeable reduction in torque density. In contrast, as shown in Fig. 5(a) and (c), when NdFeB is used for the outer rotor PM, the torque density reduction rate decreases to approximately 40%. This is because, when PM with higher MMF is placed near the bridge, it can sufficiently saturate the bridge and thereby mitigate the influence of flux leakage. Therefore, in the case of the middle bridge, since it is equally affected by both the inner and outer PMs, the required stack length increases in proportion to the total MMF.

In conclusion, the inner bridge configuration consistently achieved higher torque density than the outer bridge because the bridge is located on the inner rotor side, which has a smaller number of poles. Notably, certain PM combinations exhibited a sharp decline in performance with the outer bridge owing to increased leakage flux when Ferrite was used near the bridge. Because this study aims to maximize the torque density, only the inner bridge configuration will be considered in subsequent sections.

IV. Comparison of PM Combinations

The difference in MMF between the inner and outer rotor PMs influences both the magnetic flux density and modulation effect. This section analyzes how these differences affect the performance characteristics. The performance of various PM material combinations across different geometries, based on the design parameter ranges in Table III, were compared. As in Section III, a total of 1120 experimental points were generated for each PM combination, consisting of 1064 points by the OLHD and 56 points by the SMDD. The analyzed performances included the stack length, efficiency, peak-to-peak torque, housing loss as a function of axial leakage flux, and active material cost.

A. Stack Length and Efficiency

With the outer and inner diameters fixed, the stack length was determined to satisfy the driving conditions of Table II, which are 2.52Nm and 333.33 rpm for the inner rotor. The distribution of the stack length and efficiency by PM combination is shown in Fig. 6, considering the iron loss and PM eddy current loss. (In this paper, PM eddy current loss is defined as not included in iron loss.) As shown in Fig. 6, the torque density is observed to be proportional to the product of the residual magnetic flux densities of the inner and outer rotor PMs. This relationship can be explained from the torque equation of the magnetic gear. The torque of the magnetic gear can be calculated from the Maxwell stress tensor as follows :

$$T = \frac{L_{stk} r^2}{\mu_0} \int_0^{2\pi} B_r(r,\theta)\, B_\theta(r,\theta)\, d\theta \tag{3}$$

$$T_{\text{avg}} = \frac{L_{stk} r^2}{\mu_0} \int_0^{2\pi} \left[B_{ir}(r,\theta)\, B_{o\theta}(r,\theta) + B_{or}(r,\theta)\, B_{i\theta}(r,\theta) \right] d\theta \tag{4}$$

where T is the torque of the CMG, T_{avg} is the average torque of the CMG, L_{stk} is the stack length of the CMG, r is the radius of the airgap, B_r and B_θ are the radial and tangential magnetic flux density of the airgap, B_{ir} and $B_{i\theta}$ are the radial and tangential magnetic flux densities in the airgap produced by the inner rotor PM, B_{or} and $B_{o\theta}$ are the radial and tangential magnetic flux densities in the airgap produced by the outer rotor PM. When the spatial harmonics of the radial and tangential magnetic flux densities in the airgap of the magnetic gear are identical, the components with the same time harmonics contribute to the average torque, while those with different time harmonics contribute to the peak-to-peak torque. In the CMG, the inner and outer rotor PMs have identical time harmonics when their spatial harmonics coincide. Therefore, as expressed in (4), the component contributing to the average torque is proportional to the product of the residual flux densities of the inner and outer rotor PMs.

It can be seen that Ferrite-Nd CMG shows the highest efficiency distribution, followed by Nd-Nd and Nd-Ferrite combinations, and Nd-Ferrite CMG shows the lowest efficiency distribution. Notably, unlike previous studies, NdFeB-based CMG shows similar efficiency to Ferrite-based CMG. This is because the results were obtained under low-speed conditions. Unlike NdFeB, Ferrite has a large electrical resistivity, so there is small PM eddy current loss, which is why Ferrite CMGs are said to be more efficient than Nd CMGs in the high speed region [11]. Fig. 7 shows the loss according to the rotation speed of the outer rotor based on the median design parameter model used in

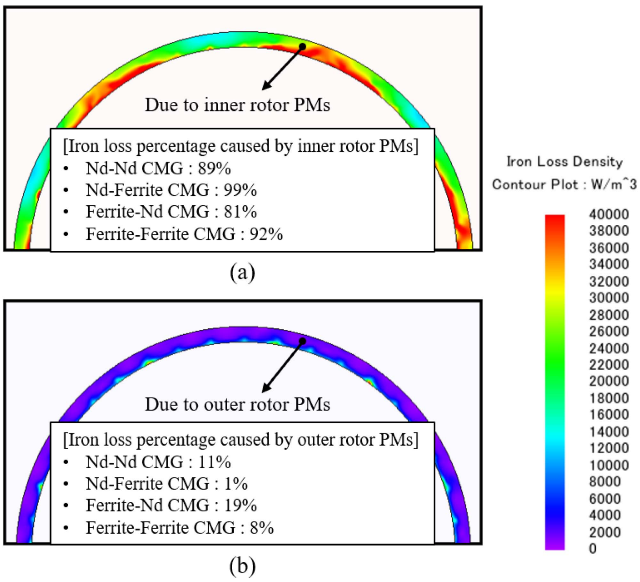

Fig. 8. Outer core iron loss distribution separated by FPM. (a) Due to inner rotor PMs. (b) Due to outer rotor PMs.

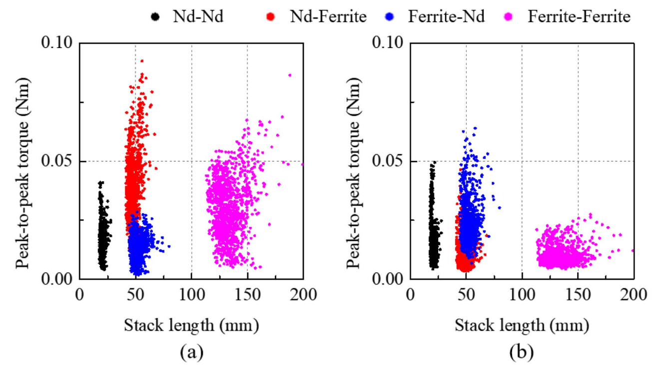

Fig. 9. Peak-to-peak torque distribution by PM combination. (a) Inner rotor. (b) Outer rotor.

Section III. Fig. 7(a) illustrates only the iron loss, and Fig. 7(b) shows the sum of the iron loss and the PM eddy current loss. (The PMs used are electrically insulated between segments, and their resistivities are listed in Table I.) The difference between Fig. 7(a) and (b) increases as the PM combination uses more Nd. As a result, when only iron loss is considered, the loss of Nd-Nd CMG is smaller than that of Ferrite-Ferrite CMG. However, when PM eddy current loss is additionally considered, the loss of Nd-Nd CMG is larger than that of Ferrite-Ferrite CMG. Based on the outer rotor speed, the difference in loss between these two combinations in Fig. 7(b) is less than 5% at 50 rpm, but it differs significantly by more than 20% at 300 rpm or higher. To reduce the PM eddy current loss, increasing the axial segmentation of the Nd makes the loss behavior in Fig. 7(b) approach that of Fig. 7(a), and the most significant effect is observed in the Nd–Nd configuration. The Nd-Ferrite combination shows a high loss even though its influence on PM eddy current is reduced like Ferrite-Nd CMG. This is due to the high iron loss characteristics, which originate from the high residual magnetic flux density of the inner rotor PM and the stack length of the Nd-Ferrite CMG. Most iron losses occurred in the modulator and outer core. At this time, the time-varying magnetic flux density of the outer rotor PMs hardly appears in the outer core. Therefore, the iron losses in the outer core primarily resulted from the time-varying modulated magnetic flux density of the inner rotor PMs. The effect of each PM on the outer core iron loss was analyzed by frozen permeability method (FPM), which allows the model to reflect the permeability in the presence of inner and outer rotor PMs. Fig. 8 shows the distribution of iron loss separated by the inner and outer rotor PMs, using the FPM for an Nd-Nd CMG model with the median design parameter model used in Section III. On average, when using the same PM, such as Nd-Nd and Ferrite-Ferrite CMGs, approximately 90% of the outer core iron loss was caused by the inner rotor PMs. For the Ferrite-Nd CMG, in which the inner rotor PMs had a smaller residual flux density than the outer rotor PMs, 81% of the iron loss was caused by the inner rotor PMs. For the Nd-Ferrite CMG, in which the inner rotor PMs had a larger residual flux density than the outer rotor PMs, 99% was caused by the inner rotor PMs. This implies that the residual magnetic flux density of the inner rotor PMs is proportional to the outer core iron loss. These analysis results explain why Nd-Ferrite CMG shows the lowest efficiency and Ferrite-Nd CMG shows the highest efficiency in Fig. 6 and Fig. 7.

B. Peak-to-Peak Torque

Since the torque of CMG changes over time, it has a maximum value and a minimum value, and the difference between them is defined as the peak-to-peak torque. Fig. 9 illustrates the peak-to-peak torque distributions of the inner and outer rotors. This distribution indicates that the Nd-Ferrite CMG has a relatively high peak-to-peak torque on the inner rotor side, while the Ferrite-Nd CMG exhibits a higher peak-to-peak torque on the outer rotor side. Unlike the average torque obtained from (4), where both the spatial and time harmonics of the radial and tangential magnetic flux densities in the airgap are identical, the peak-to-peak torque occurs when the spatial harmonics coincide, but the time harmonics differ. Therefore, among the components in (3), the interaction between the inner rotor PMs or between the outer rotor PMs generates the peak-to-peak torque component. According to [25], the peak-to-peak torque of the inner rotor is given by :

$$nU = (k_1 - k_2)N_s = (m_1 + m_2)pp_i. \tag{5}$$

$$\begin{aligned} T_{\text{pp,in}} &= \frac{L_{stk}r^2}{\mu_0}\int_0^{2\pi}\Big[B_{ir}(r,\theta)\,B_{i\theta}(r,\theta)\Big]d\theta \\ &= \frac{L_{stk}r^2}{4}\sum_{n=1}^{\infty}\Big[(\lambda_{ak_1\_\text{in}}B_{rm_1\_\text{in}} - \lambda_{bk_1\_\text{in}}B_{\theta m_1\_\text{in}}) \\ &\quad \times (\lambda_{ak_2\_\text{in}}B_{rm_2\_\text{in}} + \lambda_{bk_2\_\text{in}}B_{\theta m_2\_\text{in}}) \\ &\quad \times \sin(nU(\omega_i t + \theta_{in}))\Big] \end{aligned}$$

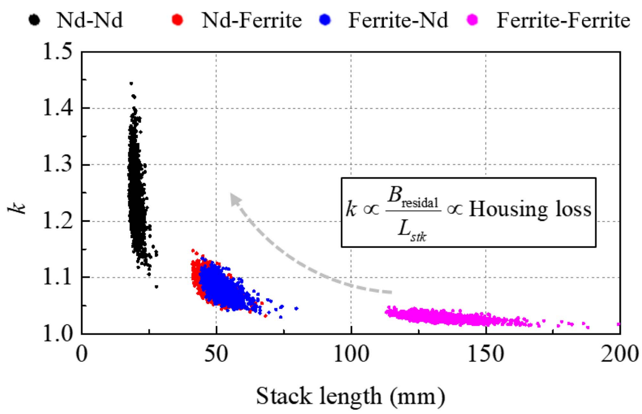

Fig. 10. Coefficient k distribution by PM combination.

$$\approx \frac{L_{stk} r^2}{4} \sum_{n=1}^{\infty} \Big[(\lambda_{ak_1\_\text{in}} B_{rm_1\_\text{in}}) \times (\lambda_{ak_2\_\text{in}} B_{rm_2\_\text{in}})$$

$$\times \sin(nU(\omega_i t + \theta_{in})) \Big]$$

$$\propto B_{r\_\text{in}} L_{stk} r^2. \tag{6}$$

where k_1 and k_2 are the spatial order of PPs relative specific permeance, m_1, and m_2 are odd and denote the spatial order of the PM field, U is the LCM of N_s and $2pp_i$, n is the any natural number, $T_{\text{pp,in}}$ is the peak-to-peak torque of the inner rotor, $\lambda_{ak_1\_\text{in}}$, $\lambda_{ak_2\_\text{in}}$, $\lambda_{bk_1\_\text{in}}$, and $\lambda_{bk_2\_\text{in}}$ are the Fourier coefficients of inner airgap relative specific permeance, $B_{rm_1\_\text{in}}$, $B_{rm_2\_\text{in}}$, $B_{\theta m_1\_\text{in}}$, and $B_{\theta m_2\_\text{in}}$ are the Fourier coefficients of the radial and the tangential components of the magnetic flux density by the inner rotor PM at inner airgap, ω_i is the rotation speed of the inner rotor, t is the time, θ_{in} is the mechanical angle of the inner rotor, B_{r_in} is the radial magnetic flux density of the inner rotor PM. When (5) is satisfied, the peak-to-peak torque is defined as in (6). Assuming that the saturation effect is ignored, the magnetic flux density of the radial component was larger than that of the tangential component at the same m_1 or m_2, and the magnetic flux density was proportional to the residual flux density of the PM. Consequently, the inner side peak-to-peak torque was proportional to the product of the stack length and the magnetic flux density of the inner rotor PM. When producing the same torque, the Nd-Ferrite CMG exhibited a larger inner rotor peak-to-peak torque than that of the Ferrite-Nd CMG. Similarly, when the residual flux densities of the inner and outer rotor PMs that produce the same torque were different, the residual flux density of the outer rotor PMs was inversely proportional to the peak-to-peak torque of the outer rotor.

C. Housing Loss as a Function of Axial Leakage Flux

Fig. 10 shows the coefficient k calculated in (2). As the k coefficient increased, a larger axial leakage flux occurred. As the end effect of the axial leakage flux diminished with increasing stack length, the distribution of k was inversely proportional to the stack length [26]. In addition, the slope of the k distribution with respect to the stack length became steeper as the residual flux density B_{residual}, increased. Axial leakage flux induced eddy current loss when housing was present along its path. As shown in Fig. 11(a), the minimum gap g_k between the active part and the end cover at which the end cover loss is negligible (less than 0.5W) under the housing material of this paper, AL6061, and the shape conditions was calculated. In order to express g_k relatively according to the stack length, the value obtained by dividing g_k by the stack length is defined as r_L, and r_L according to k is shown in Fig. 11(b). As shown in Fig. 11(b), it can be confirmed that r_L is proportional to k. Although the slopes of the relationship between k and r_L are similar, the intercept of r_L varies depending on the PM combination. This is because end cover loss is influenced not only by axial leakage flux but also partly by radial leakage flux. As a result, the r_L intercept increases in proportion to the degree of magnetic saturation in the outer core. For the Nd-Nd CMG, both the high value of k and the severe saturation of the outer core result in a required r_L that exceeds the stack length. In other words, to make the end cover loss negligible in this case, a housing height nearly twice the stack length would be necessary, which significantly lowers the torque density when the housing volume is included. Among the PM combinations using Ferrite, Nd-Ferrite, which

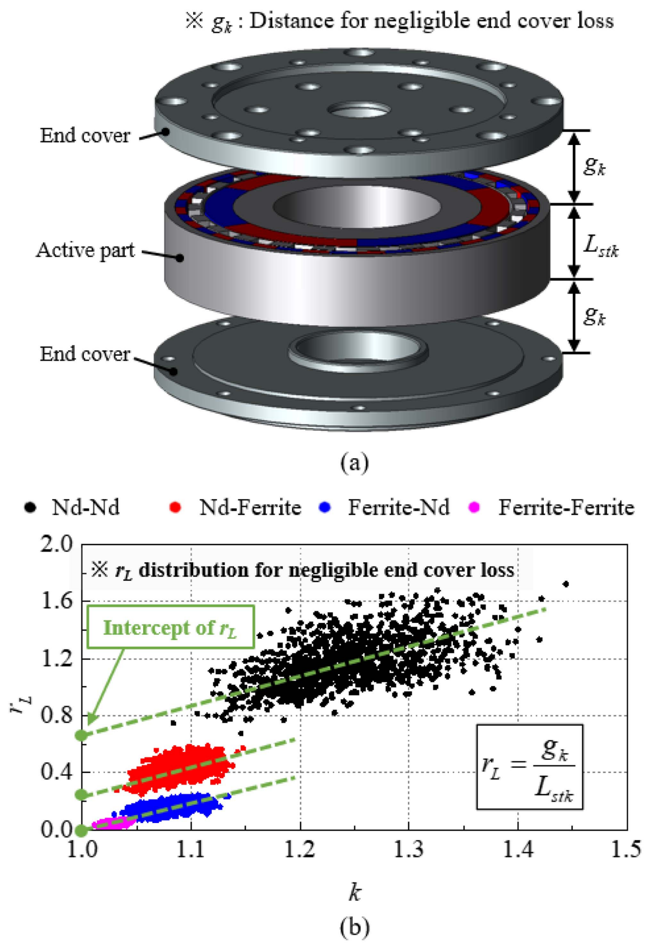

Fig. 11. Appropriate distance between the active part and the end cover to neglect end cover loss. (a) Absolute distance g_k. (b) Relative distance r_L distribution by PM combination.

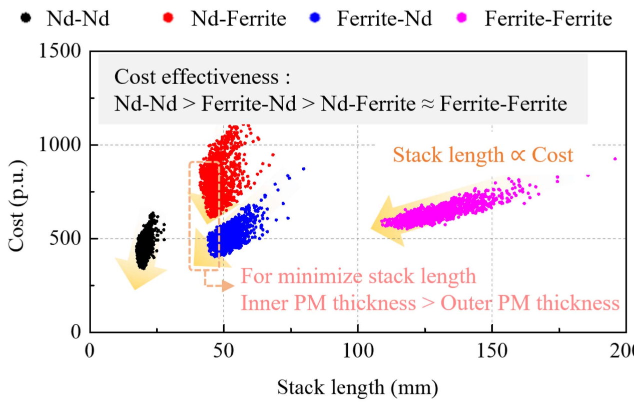

Fig. 12. Active material cost distribution by PM combination.

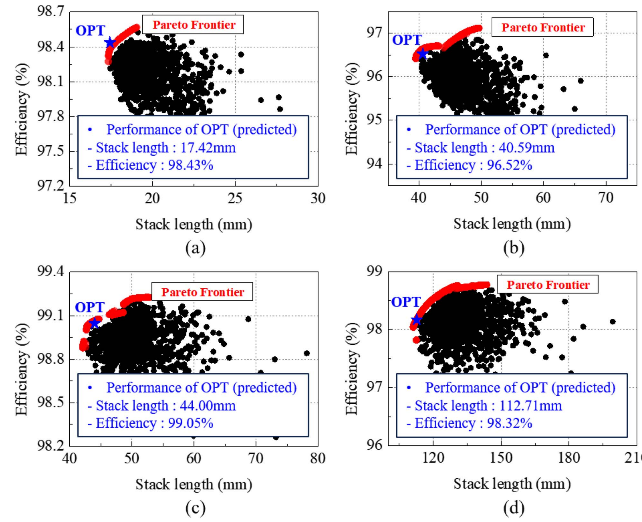

Fig. 13. Pareto Frontier. (a) Nd-Nd, (b) Nd-Ferrite, (c) Ferrite-Nd, and (d) Ferrite-Ferrite CMG.

has a high outer core saturation, has a relatively high r_L intercept. However, Ferrite-Nd and Ferrite-Ferrite CMGs have low k and r_L intercepts, which are advantageous for housing loss.

D. Active Material Cost

Fig. 12 illustrates the cost analysis for each material combination, considering only the price of active materials without accounting for manufacturing cost variations. The cost analysis was based on the unit prices provided in Table I. When NdFeB was replaced with Ferrite, the price per unit volume decreased. However, the overall material cost increased with the stack length. Consequently, the material costs for Nd-Ferrite and Ferrite-Ferrite CMGs are actually higher than those for Nd-Nd CMGs. Conversely, the cost distribution for Ferrite-Nd CMGs remained comparable to that of Nd-Nd CMGs. As shown in Table III, to maximize the torque density, the inner rotor PM was thicker than that of the outer rotor PMs. This configuration makes Ferrite-Nd CMGs cost-effective by using Ferrite in areas with a larger PM volume and NdFeB in areas with a smaller PM volume. Furthermore, regardless of the PM combination, the cost is proportional to the stack length. Therefore, when the stack length is reduced, the cost is also reduced, so the cost is not considered separately in the optimization objective function in the next section.

V. Optimal Design Models

To derive the optimal design model for each PM combination and to compare their performances, an optimization process was conducted. The overall optimal design process is illustrated in Fig. 3. As in the previous section, a total of 1120 experimental points (1064 by OLHD and 56 by SMDD) were generated for each PM combination within the design variable ranges listed in Table III. A kriging surrogate model was created based on the results of the experimental points presented in Section IV. To evaluate the accuracy of the surrogate model, the dataset was divided into five folds for cross-validation, and the normalized root mean square error (NRMSE) was assessed by sequentially using each fold as the test data. As a result, the NRMSE values for stack length and efficiency were 1.10% and 1.59% for the Nd–Nd

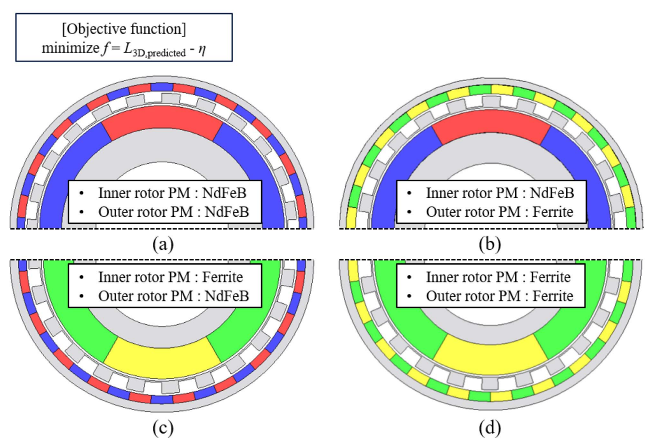

Fig. 14. 2D configurations of optimized CMG. (a) Nd-Nd, (b) Nd-Ferrite, (c) Ferrite-Nd, and (d) Ferrite-Ferrite CMG.

CMG, 0.99% and 1.33% for the Nd–Ferrite CMG, 1.11% and 1.20% for the Ferrite–Nd CMG, and 1.02% and 0.96% for the Ferrite–Ferrite CMG, respectively, confirming the high accuracy of the surrogate model. Subsequently, the design model with the minimum stack length and maximum efficiency (η) was optimized in the surrogate model through sequential quadratic programming. Fig. 13 shows the Pareto Frontier, optimum point, and the performance distribution of the experimental points. It can be observed that the Pareto Frontier appears slightly non-smooth in some cases. This is because, within the outer and inner diameter constraints specified in Table II, there was a limitation in increasing the upper bounds of the design variables in order to ensure a manufacturable inner rotor core thickness and to maintain consistent design variable ranges across all PM combinations. The optimized 2D configurations for each PM combinations are shown in Fig. 14. The optimization design parameters are listed in Table IV. For optimized models, eddy current loss in the mechanical part caused by leakage flux was

TABLE IV
DESIGN VARIABLES OF OPTIMAL DESIGNS. MINIMIZE $f = L_{3D,PREDICTED} - \eta$

PM combination	X1 (°)	X2 (mm)	X3 (mm)	X4 (mm)	X5 (mm)
Nd-Nd	7.9	8.0	2.9	3.7	2.5
Nd-Ferrite	8.0	8.3	3.4	4.1	2.5
Ferrite-Nd	7.7	11.1	3.0	4.5	3.0
Ferrite-Ferrite	7.4	11.1	3.4	4.6	3.2

TABLE V
ELECTROMAGNETIC PERFORMANCE OF OPTIMAL DESIGNS

Inner rotor target torque : 2.52 Nm
Inner rotor target rotation speed : 333.33 rpm

PM combination	L_{stk} (mm)	$T_{PP,in}$ (Nm)	$T_{PP,out}$ (Nm)	η[w/o W_H] (%)	η[w/ W_H] (%)
Nd-Nd	16.5	0.041	0.031	98.08	87.39
Nd-Ferrite	41.7	0.283	0.028	96.47	87.86
Ferrite-Nd	45.8	0.015	0.066	98.92	98.22
Ferrite-Ferrite	113	0.098	0.031	97.96	97.82

considered. Apart from the active part, the non-magnetic mechanical components that could potentially cause eddy current losses include the housing and the PPs cover, which connects and fixes the pole pieces to the housing. In this study, AL6061 aluminum alloy was used for the housing, and SUS304 stainless steel was used for the PPs cover. Although SUS304 has an electrical resistivity approximately 20 times higher than that of AL6061, it has a density nearly three times greater and is more expensive. Therefore, AL6061 was selected for the housing to minimize weight and cost, while SUS304 was chosen for the PPs cover to suppress eddy current losses. As a result, the eddy current losses generated in the PPs cover were negligible and thus excluded from the loss analysis. Therefore, only the housing loss was considered for the eddy current loss of the mechanical part, and in order to analyze the aspect under the same housing conditions, the outer and inner diameters of the housing, as well as the axial length and thickness far from the active part, were consistent across all material combinations. The distance between the active part and the end cover is 12 mm, which may be greater or less than the appropriate r_L in Fig. 11(b) for each PM combination, but was selected to evaluate the performance of each PM combination under the same conditions. Under these conditions, the optimally designed models were compared in terms of electromagnetic performance and cost-effectiveness to identify the configuration with the best Ferrite usability.

A. Electromagnetic Performance

The electromagnetic performance of the optimal design models, evaluated using 3D FEA, are summarized in Table V. The results were almost identical with the performance prediction values from the surrogate model shown in Fig. 13, with an error of less than 5%. The stack length varied with the residual flux density of the PMs. The efficiency η, calculated based on the losses in Fig. 15, was provided for the optimized models both with and without the housing loss W_H. The efficiency, without considering the housing loss trends shown in Fig. 15, were consistent with those in Fig. 6. The PM eddy current

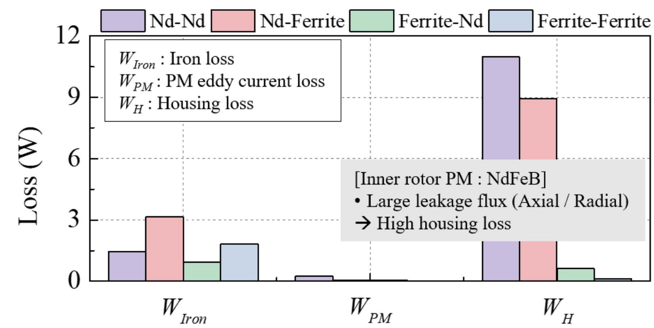

Fig. 15. Loss components of optimal model.

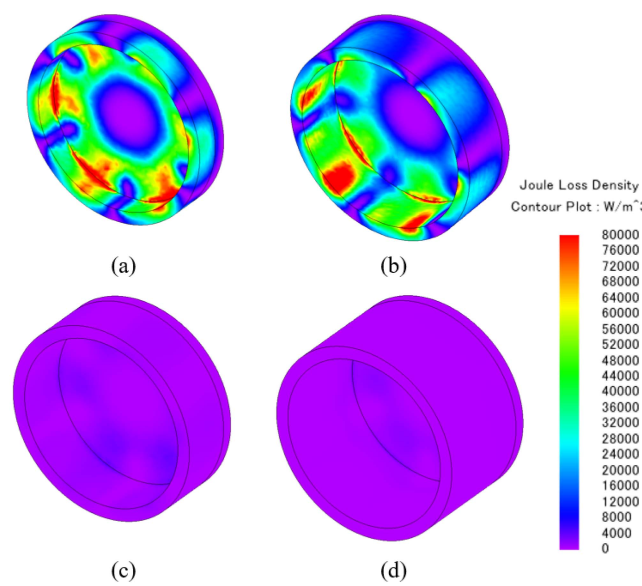

Fig. 16. Housing loss distribution of (a) Nd-Nd, (b) Nd-Ferrite, (c) Ferrite-Nd, and (d) Ferrite-Ferrite CMG.

losses remained negligible at the evaluated speed conditions. However, as illustrated in Fig. 16, the housing loss significantly affected the efficiency of combinations using NdFeB in the inner rotor PM, given the specified housing configuration. It was because the appropriate gap between the active part and the end cover calculated in Fig. 11(b) was not satisfied. The value of the distance between the active part and the end cover of the optimized model divided by the stack length is 0.73 for Nd-Nd, 0.29 for Nd-Ferrite, 0.26 for Ferrite-Nd, and 0.11 for Ferrite-Ferrite. Optimized Ferrite-Nd and Ferrite-Ferrite CMG have k of 1.10 and 1.04, respectively, referring to Fig. 11(b), which can sufficiently ignore end cover loss. However, Nd-Nd and Nd-Ferrite CMGs have k of 1.24 and 1.10, respectively, which require larger r_L in the corresponding PM combination. To reduce the housing loss while retaining housing specifications, either X2 would need to be reduced or X5 increased, both of which would lower the torque density. Under the given conditions, the optimal design of the Ferrite-Nd model achieved the highest efficiency, followed by the Ferrite-Ferrite model, in

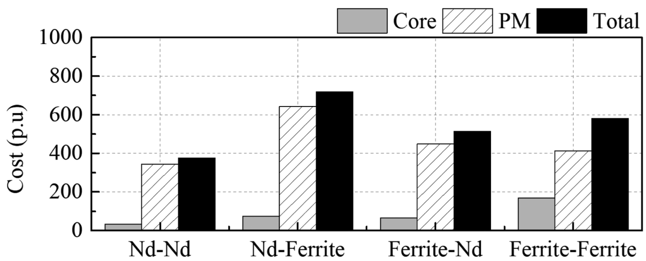

Fig. 17. Active material cost calculation of optimal designs.

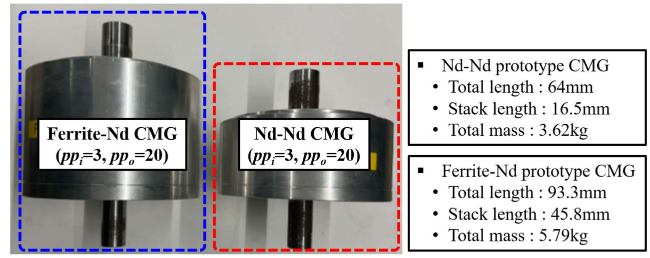

Fig. 18. Prototype of CMG.

contrast to Fig. 6, which considered the iron and PM eddy current loss.

Finally, the peak-to-peak torque was higher for the rotor using NdFeB when NdFeB and Ferrite were used together, which was consistent with the results observed in the 2D FEA.

B. Cost Effectiveness

A comparison of prices at the maximum torque density and efficiency, as shown in Fig. 11, confirms that the Ferrite-Nd model was similar in cost to the Nd-Nd model. Supporting this observation, the active material cost analysis of the optimal design models is shown in Fig. 17. Among the designs using Ferrite, the Ferrite-Nd model was the most cost-effective. Given the rising cost of rare earth materials, the Ferrite-Nd model remains a competitive option that reduces the rare earth dependency while maintaining comparable costs.

VI. Experimental Validation

In the previous section, the electromagnetic performance and active material costs of optimized models for each PM material combination were compared. Overall, the Ferrite-Nd model demonstrated superior performance among the configurations using Ferrite. Therefore, in this section, the conventional Nd-Nd model and a newly proposed PM combination, the Ferrite-Nd model, were fabricated and tested. Prior to fabrication, high-speed structural analysis and high-temperature demagnetization analysis were conducted on the models. Structural analysis confirmed that sufficient rigidity was satisfied under the test load conditions, and irreversible demagnetization appeared at around 70 degrees for Nd-Nd CMG and around 110 degrees for Ferrite-Nd CMG. Demagnetization mostly occurs in the outer rotor PM. Therefore, Ferrite-Nd CMG showed favorable results in demagnetization characteristics because the MMF of the inner rotor PM was small. Fig. 18 shows prototypes of the optimized models along with their lengths and weights. Total length represents the length including the housing, stack length represents the length of the active part excluding the housing, and total mass represents the weight of the prototype. (Total length does not include shaft length.) The housings of the two prototype CMGs are designed with the same thickness and distance from the active part (12 mm on one side in the axial direction and 5.5 mm on one side in the radial direction), so that the height and radius increase due to the housing are the same. Fig. 19 depicts the experimental setup. In this set of experiments, Fig. 20 and 21 show the torque and speed results for the prototype Nd-Nd and Ferrite-Nd models, respectively. Table VI summarizes the results. To conduct the test under conditions matching the simulation, the inner rotor was driven at 2.50 Nm and 333.33 rpm. Under these inner rotor driving conditions , the outer rotors were all driven at 50 rpm according to the gear ratio. However, the torque ratio decreased from 6.67 due to losses. Fig. 22 compares the loss components and efficiency between the 3D FEA and experimental results. The predicted mechanical loss was calculated by subtracting the housing, PM eddy current, and iron losses from the experimental total loss $W_{Experiment}$. As previously shown, the iron and PM eddy current losses of the prototype Nd-Nd and Ferrite-Nd CMGs were comparable, while housing losses accounted for a substantial efficiency difference. These experimental findings agree with the efficiency values listed in Table V.

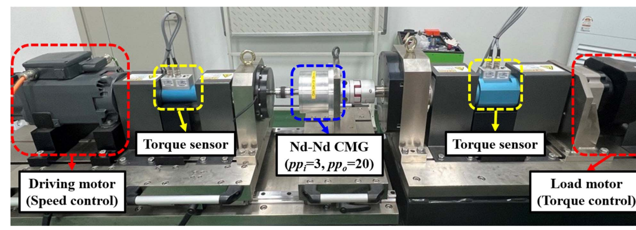

Fig. 19. Experiment setup.

TABLE VI
Experimental Data of Prototypes

Electromagnetic performance	Nd-Nd CMG	Ferrite-Nd CMG	Unit
Inner / Outer rotor speed	333.33 / 50	333.33 / 50	rpm
Inner rotor average torque	2.50	2.50	Nm
Outer rotor average torque	13.55	15.92	Nm
Specific torque	3.74	2.75	Nm/kg
Volumetric torque density	13.75	11.08	kNm/m^3
Inner rotor peak-to-peak torque	0.13	0.23	Nm
Outer rotor peak-to-peak torque	1.18	1.10	Nm
Efficiency	81.30	95.52	%

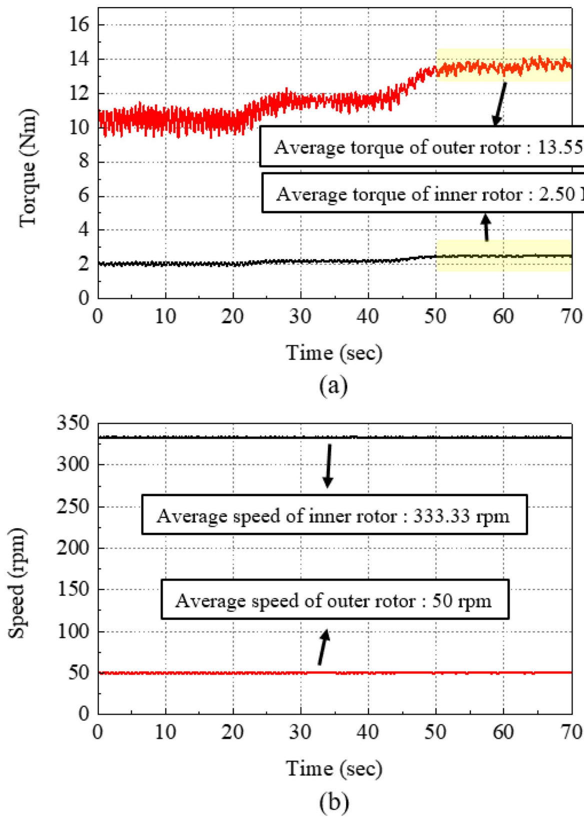

Fig. 20. Experimental data of prototype Nd-Nd CMG. (a) Torque data. (b) Speed data.

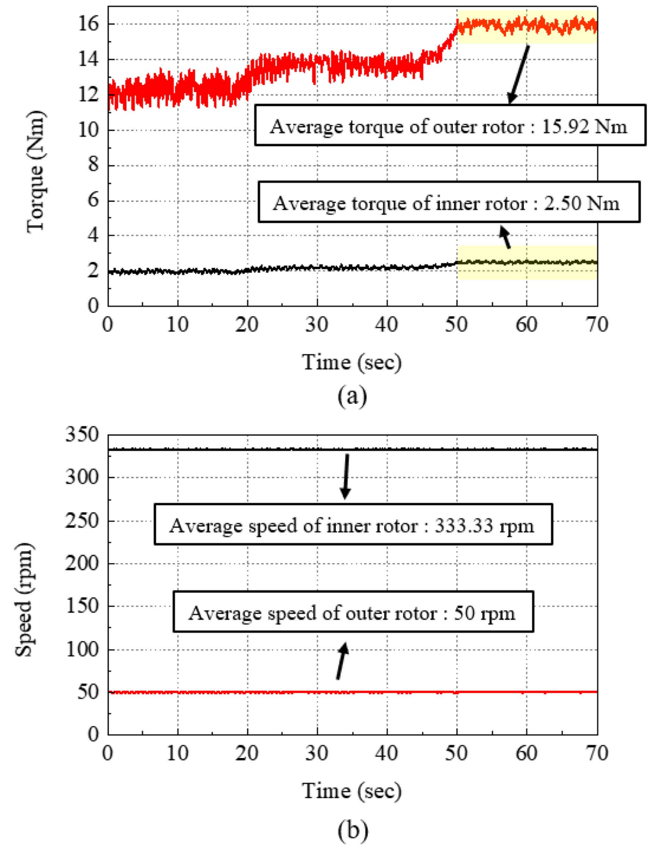

Fig. 21. Experimental data of prototype Ferrite-Nd CMG. (a) Torque data. (b) Speed data.

The efficiency difference between Nd-Nd CMG and Ferrite-Nd CMG also affected the torque density. As shown in Fig. 18, the stack length and the total length including the housing are about 2.8 times and 1.46 times larger for the Ferrite-Nd model, respectively. However, due to the decrease in outer rotor torque of Nd-Nd CMG caused by the low efficiency, the specific torque in Table VI is 1.36 times and the volumetric torque density (VTD) is 1.24 times, which is a small difference compared to the increase in length. Specific torque was calculated by dividing the total mass from the outer rotor average torque, and the VTD was calculated from the following formula, reflecting the volume including the housing.

$$\mathrm{VTD} = \frac{\text{Outer rotor average torque}}{\pi \times (\text{Outer radius})^2 \times (\text{Total length})} \qquad (7)$$

Differences between the peak-to-peak torque in the experiment and simulation were observed. Unlike in the simulation, the CMG did not operate in isolation during the experiment and was influenced by the operating system. Because the peak-to-peak torque of the CMG was significantly smaller than that of the drive motor, the torque ripple for both prototypes were measured at similar levels.

Although it is difficult to verify the peak-to-peak torque difference, it can be experimentally proven that the efficiencies of the fabricated Nd-Nd and Ferrite-Nd CMGs differed owing to housing loss.

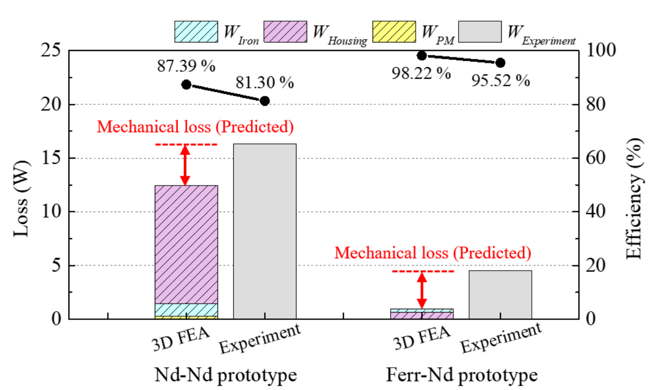

Fig. 22. Comparison of 3D FEA and experiment of loss components and efficiency.

VII. Conclusion

In this study, CMGs with four different PM combinations were proposed and evaluated. Each combination was designed through an optimal design process utilizing an EMC equivalent to 3D analysis. First, the optimal bridge shape for each PM combination was analyzed, revealing that the inner bridge consistently achieved higher torque density regardless of the PM combination. Next, the usability of Ferrite was assessed by examining the performance distribution across experimental points. The simulation results indicated that differences in the MMF between the inner and outer rotor PMs led to variations in the torque density, active material cost, iron loss, peak-to-peak torque, and leakage flux. The key findings include the following: (1) Torque is proportional to the product of the residual flux densities of the inner and outer PMs, respectively. (2) Through the FPM, it was validated that an increase in the MMF of the inner rotor PM resulted in a higher iron loss. (3) When the PM materials of the inner and outer rotors differ, the peak-to-peak torque was higher for rotors with higher residual flux densities. (4) The gap between the active part and the end cover was calculated to be at a level where the end cover loss is negligible according to k for each PM combination. In the case of Nd-based CMG, the leakage flux is large, so a larger relative gap is required than that of CMG using Ferrite. Overall, the Ferrite-Nd CMG emerged as the most promising material combination using nonrare earth PM. Finally, prototypes of the optimized Nd-Nd and Ferrite-Nd CMGs were fabricated and tested. Unlike the Ferrite-Nd model, the Nd-Nd CMG exhibited a notable housing loss. To mitigate housing losses, the design must either be adjusted to reduce leakage, which may occur at the expense of torque density, or the housing size must be increased both axially and radially.

The Ferrite-Nd combination showed high efficiency compared to Nd-Nd CMG, and the price difference is not large. Considering the increase in inactive housing volume required to reduce housing loss and the rising cost of rare earth PMs, Ferrite-Nd CMG presents a promising alternative to replace existing CMGs.

References

[1] J. J. Scheidler, V. M. Asnani, and T. F. Tallerico, "NASA's magnetic gearing research for electrified aircraft propulsion," in *Proc. AIAA/IEEE Electr. Aircr. Technol. Symp.*, Jul. 2018, pp. 1–12.

[2] L. Jian and K. T. Chau, "A novel electronic-continuously variable transmission propulsion system using coaxial magnetic gearing for hybrid electric vehicles," *J. Asian Electr. Veh.*, vol. 7, no. 2, pp. 1291–1296, 2009.

[3] K. K. Uppalapati, J. Z. Bird, D. Jia, J. Garner, and A. Zhou, "Performance of a magnetic gear using ferrite magnets for low speed ocean power generation," in *Proc. IEEE Energy Convers. Congr. Expo.*, 2012, pp. 3348–3355.

[4] M. Filippini and P. Alotto, "Coaxial magnetic gear design and optimization," *IEEE Trans. Ind. Electron.*, vol. 64, no. 12, pp. 9934–9942, Dec. 2017.

[5] M. Chen, K. T. Chau, W. Li, and C. Liu, "Cost-effectiveness comparison of coaxial magnetic gears with different magnet materials," *IEEE Trans. Magn.*, vol. 50, no. 2, pp. 821–824, Feb. 2014.

[6] K. Aiso, K. Akatsu, and Y. Aoyama, "A novel reluctance magnetic gear for high-speed motor," *IEEE Trans. Ind. Appl.*, vol. 55, no. 3, pp. 2690–2699, May/Jun. 2019.

[7] S. A. Khan and M. C. Gardner, "Development and analysis of a homopolar consequent pole transverse flux magnetic gear," in *Proc. IEEE Int. Electric Machines Drives Conf.*, 2023, pp. 1-7.

[8] S. A. Afsari Kashani, "Design and optimization of coaxial reluctance magnetic gear with different rotor topologies," *IEEE Trans. Ind. Electron.*, vol. 69, no. 1, pp. 101–109, Jan. 2022.

[9] Z. Q. Zhu, X. Liu, and Z. Pan, "Analytical model for predicting maximum reduction levels of vibration and noise in switched reluctance machine by active vibration cancellation," *IEEE Trans. Energy Convers.*, vol. 26, no. 1, pp. 36–45, Mar. 2011.

[10] M. Johnson, M. C. Gardner, and H. A. Toliyat, "Design comparison of NdFeB and ferrite radial flux surface permanent magnet coaxial magnetic gears," *IEEE Trans. Ind. Appl.*, vol. 54, no. 2, pp. 1254–1263, Mar./Apr. 2018.

[11] E. Park, S. Jung, and Y. Kim, "Comparison of magnetic gear characteristics using different permanent magnet materials," *IEEE Trans. Appl. Supercond.*, vol. 30, no. 4, pp. 1–4, Jun. 2020.

[12] K. K. Uppalapati, W. B. Bomela, J. Z. Bird, M. D. Calvin, and J. D. Wright, "Experimental evaluation of low-speed flux-focusing magnetic gearboxes," *IEEE Trans. Ind. Appl.*, vol. 50, no. 6, pp. 3637–3643, Nov./Dec. 2014.

[13] A. Al-Qarni, F. Wu, and A. Ei-Refaie, "High-torque-density low-cost magnetic gear utilizing hybrid magnets and advanced materials," in *Proc. IEEE Int. Electr. Mach. Drives Conf.*, May 2019, pp. 225–232.

[14] P. O. Rasmussen, T. O. Andersen, F. T. Jorgensen, and O. Nielsen, "Development of a high-performance magnetic gear," *IEEE Trans. Ind. Appl.*, vol. 41, no. 3, pp. 764–770, May/Jun. 2005.

[15] B.-C. Bae, S.-Y. Im, S.-H. Lee, and M.-S. Lim, "Comparison of coaxial magnetic gears using rare earth and nonrare earth permanent magnets," in *Proc. 2023 IEEE Transp. Electrific. Conf. Expo*, 2023, pp. 1–6.

[16] B. Praslicka, M. C. Gardner, M. Johnson, and H. A. Toliyat, "Review and analysis of coaxial magnetic gear pole pair count selection effects," *IEEE J. Emerg. Sel. Topics Power Electron.*, vol. 10, no. 2, pp. 1813–1822, Apr. 2022.

[17] G. Jungmayr, J. Loeffler, B. Winter, F. Jeske, and W. Amrhein, "Magnetic gear: Radial force, cogging torque, skewing, and optimization," *IEEE Trans. Ind. Appl.*, vol. 52, no. 5, pp. 3822–3830, Sep./Oct. 2016.

[18] S. Gerber and R.-J. Wang, "Evaluation of a prototype magnetic gear," in *Proc. IEEE Int. Conf. Ind. Technol.*, Feb. 2013, pp. 319–324.

[19] S.-H. Lee, S.-Y. Im, J.-Y. Ryu, and M.-S. Lim, "Optimum design process of coaxial magnetic gear using 3D performance prediction method considering axial flux leakage," *IEEE Trans. Ind. Appl.*, vol. 60, no. 2, pp. 3075–3085, Mar./Apr. 2024.

[20] S.-Y. Im, S.-G. Lee, D.-M. Kim, G. Xu, S.-Y. Shin, and M.-S. Lim, "Kriging surrogate model-based design of an ultra-high-speed surface-mounted permanent-magnet synchronous motor considering stator iron loss and rotor eddy current loss," *IEEE Trans. Magn.*, vol. 58, no. 2, pp. 1–5, Feb. 2022.

[21] Y. Zhan, L. Ma, K. Wang, H. Zhao, G. Xu, and N. Ding, "Torque analysis of concentric magnetic gear with interconnected flux modulators," *IEEE Trans. Magn.*, vol. 55, no. 6, pp. 1–4, Jun. 2019.

[22] K. K. Uppalapati and J. Z. Bird, "An iterative magnetomechanical deflection model for a magnetic gear," *IEEE Trans. Magn.*, vol. 50, no. 2, pp. 245–248, Feb. 2014.

[23] M. Johnson, M. C. Gardner, H. A. Toliyat, S. Englebretson, W. Ouyang, and C. Tschida, "Design, construction, and analysis of a large-scale inner stator radial flux magnetically geared generator for wave energy conversion," *IEEE Trans. Ind. Appl.*, vol. 54, no. 4, pp. 3305–3314, Jul./Aug. 2018.

[24] J. D. Kyu and C. J. Hwan, "Effect of stationary pole pieces with bridges on electromagnetic and mechanical performance of a coaxial magnetic gear," *J. Magn.*, vol. 18, no. 2, pp. 207–211, 2013.

[25] L. Jian and K. Chau, "A coaxial magnetic gear with halbach permanent-magnet arrays," *IEEE Trans. Energy Convers.*, vol. 25, no. 2, pp. 319–328, Jun. 2010.

[26] M. C. Gardner, B. E. Jack, M. Johnson, and H. A. Toliyat, "Comparison of surface mounted permanent magnet coaxial radial flux magnetic gears independently optimized for volume, cost, and mass," *IEEE Trans. Ind. Appl.*, vol. 54, no. 3, pp. 2237–2245, May/Jun. 2018.

Byeong-Cheol Bae received the bachelor's degree in automotive engineering in 2023 from Hanyang University, Seoul, South Korea, where he is currently working toward the Ph.D. degree in automotive engineering. His research interests include design and optimization of electric machines and analysis of electro-magnetic field.

Seung-Hun Lee received the bachelor's degree in automotive engineering in 2022 from Hanyang University, Seoul, South Korea, where he is currently working toward the Ph.D. degree in automotive engineering. His research interests include design and optimization of electric machines and analysis of electro-magnetic field.

So-Yeon Im received the bachelor's degree in automotive engineering in 2020 from Hanyang University, Seoul, South Korea, where she is currently working toward the Ph.D. degree in automotive engineering. Her research interests include the optimization, design, and system modeling of electric vehicles.

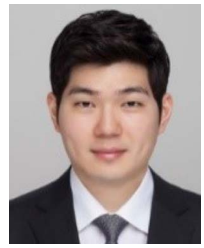

Myung-Seop Lim (Senior Member, IEEE) received the bachelor's degree in mechanical engineering and the master's and Ph.D. degrees in automotive engineering from Hanyang University, Seoul, South Korea, in 2012, 2014 and 2017, respectively. From 2017 to 2018, he was a Research Engineer in Hyundai Mobis, Yongin, South Korea. From 2018 to 2019, he was an Assistant Professor in Yeungnam University, Daegu, South Korea. Since 2019, he has been with Hanyang University, where he is currently an Assistant Professor. His research interests include electromagnetic field analysis and multi-physics analysis of electric machinery for mechatronics systems such as automotive and robot applications.